JOURNAL OF PROPULSION AND POWER
Vol. 22, No. 3, May–June 2006

Experimental and Numerical Study of a Dual-Mode Scramjet Combustor

C. P. Goyne*
University of Virginia, Charlottesville, Virginia 22904
C. G. Rodriguez†
ATK-GASL, Hampton, Virginia 23681
R. H. Krauss‡ and J. C. McDaniel§
University of Virginia, Charlottesville, Virginia 22904-4248
and
C. R. McClinton¶
NASA Langley Research Center, Hampton, Virginia 23681

A Mach 2, hydrogen-air combustor with an unswept 10-deg ramp fuel injector was experimentally and numerically studied for a simulated flight Mach number near 5. Numerical modeling was performed using the Viscous Upwind Algorithm for Complex Flow Analysis code, and results were compared against experimental wall-pressure distributions, fuel plume images, and fuel plume velocity measurements. The model matched wall-pressure distributions well for the case of fuel-off and fuel-air mixing. For a fuel-air reacting case, pressure was matched well in the upstream third of the duct. Downstream, however, the pressure rise as a result of combustion was underpredicted. Based on the fuel plume imaging and velocity measurements, fuel plume shape was matched well for both the mixing and reacting cases. However, plume size, penetration, and centerplane axial growth were generally underpredicted by the model. The full extent of the velocity reduction caused by thermal choking was also not predicted. Despite these findings, the numerical model performed better than a previous model developed by the investigators. It was proposed that differences between the present numerical model and experiment stemmed from numerical underprediction of fuel-air turbulent mixing, and this resulted in underprediction of heat release.

Nomenclature

H	=	normal height of ramp fuel injector
P	=	pressure
Pr	=	Prandtl number
Sc	=	Schmidt number
T	=	temperature
X, Y, Z	=	Cartesian coordinates with origin at ramp base
y^+	=	inner-law variable
μ	=	viscosity
τ	=	turbulence intensity

Subscripts

L	=	laminar
pitot	=	pitot quantity
ref	=	reference quantity at nozzle exit
T	=	turbulent
t	=	total
0	=	stagnation quantity

Presented as Paper 2002-5216 at the AIAA/AAAF 11th International Space Planes and Hypersonic Systems and Technologies Conference, Orleans, 29 September–4 October 2002; received 15 September 2004; revision received 29 July 2005; accepted for publication 12 August 2005. Copyright © 2005 by the American Institute of Aeronautics and Astronautics, Inc. All rights reserved. Copies of this paper may be made for personal or internal use, on condition that the copier pay the $10.00 per-copy fee to the Copyright Clearance Center, Inc., 222 Rosewood Drive, Danvers, MA 01923; include the code 0748-4658/06 $10.00 in correspondence with the CCC.

*Research Assistant Professor, Department of Mechanical and Aerospace Engineering. Senior Member AIAA.
†Senior Engineer; currently Assistant Professor, Departamento de Ingenieria Mecanica, Casilla 160, Universidad de Concepcion, Concepcion, Chile. Senior Member AIAA.
‡Research Consultant, Aerospace Research Laboratory.
§Professor, Department of Mechanical and Aerospace Engineering. Senior Member AIAA.
¶Retired Manager, Flight Vehicles and Systems Program Office, MS 353X. Senior Member AIAA.

Introduction

ALTHOUGH dual-mode scramjets continue to be at the core of propulsion concepts for hypersonic access to space, dual-mode combustor design tools currently lack the level of maturity that has been achieved for other scramjet components such as inlets and exhaust nozzles.[1] Even though the dual-mode combustor of NASA's X-43A flight-test vehicle, for example, saw extensive ground-based testing and computational-fluid-dynamics (CFD) analyses, full three-dimensional CFD played a secondary role in combustor design, optimization, and performance prediction. Furthermore, ground-based combustor tests suffered from the effects of facility contaminants, such as heater vitiates, and these effects had to be included in combustor design and analysis.[2,3] Such effects further hinder gains made towards improving CFD predictive capabilities. To address these issues, an experimental and numerical study of a dual-mode scramjet combustor has been undertaken. Using a simplified three-dimensional combustor geometry, which simplifies the numerical modeling, and an electrically heated supersonic combustion facility, which provides a test gas free of contaminants, the study aims to use CFD validation to improve the accuracy of numerical predictions of the fuel-air mixing and combustion processes in a dual-mode scramjet combustor.

The experimental component of the study is aimed at generating a comprehensive benchmark data set through the use of conventional instrumentation and multiple laser-based diagnostics.[4–7] The dual-mode scramjet under investigation is a direct-connect Mach 2 hydrogen-air combustor with a single 10-deg unswept-ramp fuel injector. The configuration results in a mixing and combusting flow that is highly three dimensional. Electrically heated air is supplied via a unique continuous-flow facility and flow conditions simulate operation of a scramjet at a flight Mach number near 5.

The numerical component of the study is part of a larger endeavor aimed at the examination of the optimum combination of codes,

grids, and turbulence and chemistry models for the simulation of dual-mode scramjet combustors.[8–10] The experimental and numerical studies are being conducted in parallel, and this arrangement has enabled rapid feedback between investigators. It is anticipated that this in turn will facilitate rapid progress towards CFD accuracy improvements.

The investigators have previously reported comparisons between experiment and CFD for the combustor. Wall-pressure measurements and fuel-plume-imaging (FPI)[6] and particle-image-velocimetry (PIV)[7] results were separately compared with a simulation performed using the GASP code.[11] The numerical model was shown to be capable of approximating the pressure distribution in the duct when combustion occurred. From the FPI measurements, it was established that the model was able to approximately match the fuel-air mixing if the combustion process were precluded. However, when combustion occurred, the model was not able to accurately predict the changes in the fuel plume size, penetration, shape, and axial growth. In terms of the velocity distribution on the centerplane of the combustor, the model was able to generally match velocity magnitudes of the reacting flowfield. However, plume penetration was again not adequately predicted.

The present contribution reports on the progress toward improving agreement between the experimental and numerical results. Experimental effort has concentrated on quantifying the combustor inflow boundary condition through total temperature and pitot-pressure surveys at the exit of the Mach 2 nozzle. The numerical component of the study has focussed on the adoption of a different CFD code and the investigation of the effects of altering boundary conditions. In particular, the Viscous Upwind Algorithm for Complex Flow Analysis (VULCAN) code[12] has been adopted, and the effects of laminar and turbulent boundary layers in the Mach 2 nozzle have been examined.

The paper begins with a description of the facility, flow conditions, and dual-mode combustor of the experiment. The technique used to obtain the nozzle survey is then presented. Because the techniques used by Refs. 6 and 7 for the FPI and PIV experiments have implications on the data interpretation and comparison with CFD, the FPI and PIV experiments are briefly described. The new numerical model is then described before moving on to compare the experimental and numerical results. As part of the comparison, the Mach 2 nozzle profiles are first examined, and then the combustor pressure and Mach-number distribution and fuel plume velocity field and distribution are explored. As both the experiment and numerical model presented the ability to preclude combustion when fuel was introduced into the combustor, the effects of combustion on the fuel-air mixing process are examined by comparing the results in terms of mixing (nonreacting) fuel air and reacting fuel air. The present study represents the first-time FPI, PIV, and pressure measurements have been simultaneously compared with a numerical simulation of a dual-mode scramjet combustor.

Experimental Technique

Facility, Flow Conditions, and Combustor

The experiments reported here were performed using the University of Virginia Supersonic Combustion Facility. The facility is schematically presented in Fig. 1a and is fully described by Refs. 13 and 14. As can be seen in the figure, the facility was vertically mounted. This facilitated unimpeded physical and optical access to the dual-mode combustor portion of the facility. Compressed air was supplied to the facility via an oil-free compressor and desiccant air dryer system. This air was then heated in a pressurized heater tank via a 300-kW, 14-stage electrical resistance heater. Cold supply air entered the top of the heater tank and flowed down the outer portion of an annular section. At the lower end of the tank, the air entered a heater core that housed the resistance heaters. The air flowed up through the core to exit from the last heater stage at a temperature approaching 1200 K. In contrast to vitiated and arc-driven facilities, the heater was able to supply a test gas that was free of contaminants such as water, NO, particles, and radical species.[13,14] After exiting the electrical resistance heater, the test air flowed through a ceramic flow straightener. It then passed through the Mach 2 nozzle

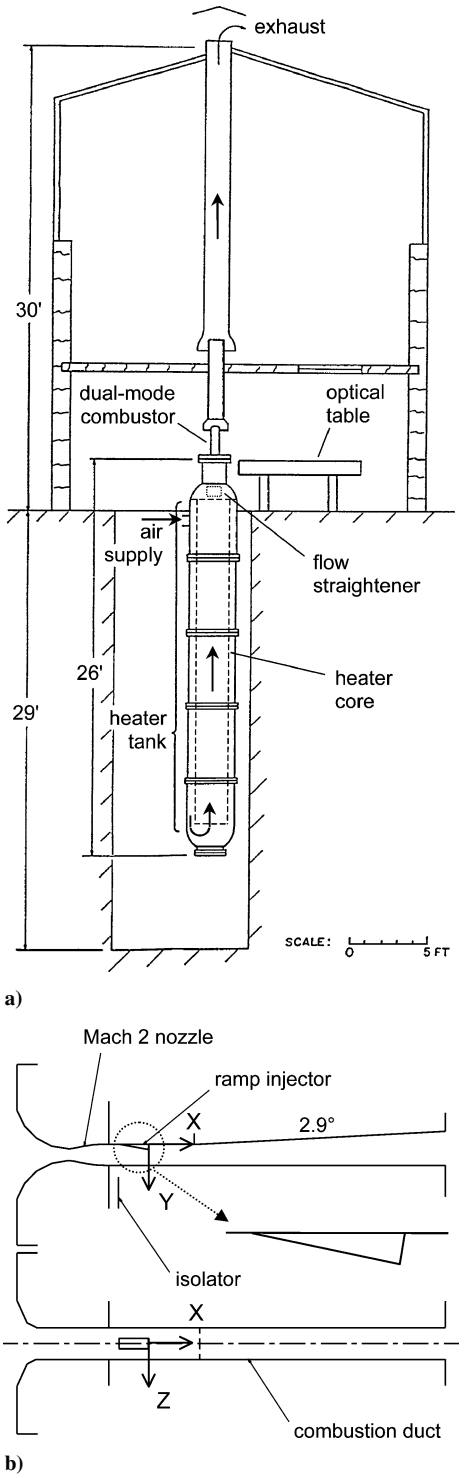

Fig. 1 Schematic of a) University of Virginia Supersonic Combustion Facility and b) dual-mode combustor.

and combustor assembly. The exit of the test section was open to the laboratory, and exhaust gases were removed from the building via an open-ended exhaust tube. A type K thermocouple probe, which was located in a plenum between the flow straightener and dual-mode combustor, served to monitor the facility's stagnation temperature. This temperature and other operating conditions are listed in Table 1.

A schematic of the dual-mode combustor, together with a definition of measurement axes, is presented in Fig. 1b. The combustor basically consisted of a two-dimensional Mach 2 nozzle, a short constant-area isolator, and a rectangular combustion duct. One of the walls of the combustor, referred to herein as the injection wall, included an unswept 10-deg compression ramp. Hydrogen fuel was introduced from the base of the ramp via a Mach 1.7 conical nozzle.

Table 1 Test conditions

Parameter	Dual-mode combustor		Nozzle survey	Error
Gas	Air	H_2	Air	——
Stag. pressure, kPa	330–390	930–1010	415	±3%
Stag. temperature, K	1120	300	1030	±3%
Mach number[a]	2.07	1.7	2.07	——
Static pressure[a], kPa	39–47	190–210	48	——
Static temperature,[a] K	650	190	600	——
Velocity,[a] m/s	1030	1760	990	——
Equivalence ratio	——	0.28	——	±5%

[a]Property at nozzle exit determined using nozzle area ratio and assuming isentropic flow.

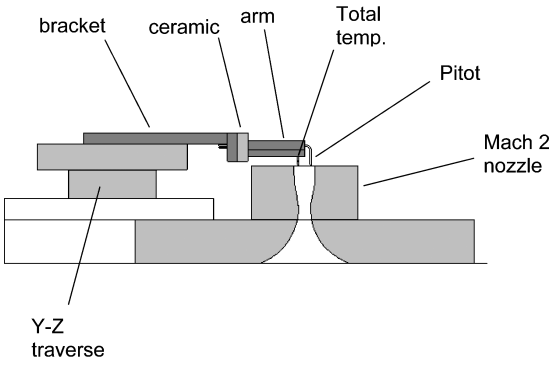

Fig. 2 Schematic of Mach 2 nozzle survey probe.

The centerline of the injection nozzle was parallel to the compression surface of the ramp. Using the normal height of the ramp ($H = 6.4$ mm) to normalize linear dimensions, the isolator and combustion duct inlet dimensions were $4H \times 6H$. From a distance of $10H$ downstream of the ramp base, the injection wall had a 2.9-deg divergence. Flow exited the combustor at $X/H = 58$. The centerline of the injection wall, through the isolator, ramp and combustion duct sections were instrumented with pressure taps. One off-axis measurement station, at $4H$ downstream of the fuel injector, consisted of two taps, $1H$ each from the wall centerline. Fueling conditions for the combustor are presented in Table 1. Once steady fuel flow was established, the combustor could be ignited using a detonation-driven igniter system. This igniter system consisted of a 1.5-m long, 25-mm i.d. stainless-steel tube with a spark plug at one end. Oxygen and hydrogen were introduced into the tube and ignited using the spark plug. The resulting combustion products were then fed into the flow immediately downstream of the fuel injector. Combustion was self-sustaining following ignition. More complete descriptions of the combustor geometry, instrumentation, fueling, optical access, and data acquisition are reported elsewhere.[6,7]

Nozzle Survey Probe

Total temperature and pitot-pressure surveys of the Mach 2 nozzle were performed using a purpose-built probe assembly that is schematically presented in Fig. 2. For these measurements, the combustion duct and isolator of Fig. 1b were removed from the Mach 2 nozzle, and the flow was interrogated on a measurement plane that was 1.7 mm downstream of the exit of the nozzle. The nozzle exhausted into the laboratory and, hence, had a backpressure near 1 atm. This level was approximately twice the nozzle backpressure for combustion tests of the dual-mode scramjet. Therefore, in order to ensure the nozzle flow was driven to a fully started condition, the facility was operated with a higher stagnation pressure than used for the scramjet tests. Operating conditions are listed in Table 1. The nozzle survey probe was built in house and consisted of a total temperature probe and a pitot tube. These components were constructed of 1.59-mm outer diameter Inconel tubing with a 0.13-mm wall. The tubes were located via a stainless-steel cantilever arm that had a 40-deg included angle sharp leading edge. The cantilever arm was mounted on a Y-Z traverse assembly using a thermal insulating, alumina silicate ceramic, and an aluminum mounting bracket. The melting temperatures of the Inconel and stainless-steel components were near 1600 K, and tests of the survey probe in the nozzle flow demonstrated that these components did not require active cooling. In addition, temperature rise of the aluminum bracket was minimal during testing. The Y-Z traverse assembly was capable of traversing the probe throughout the nozzle flow with a resolution of 1 μm at an absolute positioning uncertainty of 0.2 mm.

The total temperature probe design was based on that of Ref. 15. The design basically consisted of a radiation-shielded type R thermocouple. The radiation shield was formed by the Inconel tubing. The main difference between the present design and that of Ref. 15 was that the radiation shield was of constant diameter, rather than having a flattened cross section at the inlet. In addition, the thermocouple wire diameter (0.2 mm) was 20% smaller in order to limit conduction losses from the thermocouple bead (~Ø 0.4 mm). A two-hole alumina ceramic insulator and high-temperature cement located and sealed the thermocouple wires in the radiation shield. The radiation shield had a vent to inlet area ratio of 50%. The vent consisted of two 0.66-mm holes that were located 180 deg apart and were 3 mm downstream of the thermocouple bead.

Based on the estimates of Ref. 15, the 99% rise time of the total temperature probe was expected to be less than 5 s with a recovery factor near unity and a temperature measurement error of a few percent. The latter analysis accounted for errors caused by flow velocity over the thermocouple bead and conduction and radiation losses.

Pitot-pressure levels were measured using a Setra™ type pressure transducer. Output of this transducer, together with the output of the total temperature thermocouple, was monitored via a Fluke Hydra Data Logger. Including measurement errors of the data-acquisition system and the transducers, experimental uncertainty in total temperature and pitot pressure were estimated to be approximately ±3 and ±2%, respectively. In addition, measured levels of total temperature and pitot pressure were typically steady to within ±2 and ±3%, respectively.

Previous FPI and PIV Experiments

The FPI and PIV experiments of Refs. 6 and 7, respectively, were performed by seeding fine particles into the hydrogen fuel stream prior to injection. The fuel-air mixing and combustion wake of the injector was then visualized by illuminating the seeded particles via a sheet of laser light. The laser sheet was oriented in the crossflow plane (at $X/H = 3$, 5, and 7) for the FPI measurements. For the PIV technique, the laser sheet was located on the centerplane of the combustor. For the latter technique, velocity information was obtained by pulsing the laser sheet twice, using a known temporal separation, and digitally determining the particle displacement between pulses via an autocorrelation technique. As only the fuel was seeded, velocity was measured only in the fuel plume.

The seed particles used for the FPI and PIV measurements consisted of silicon dioxide (SiO_2) and alumina (Al_2O_3) powder, respectively, with manufacturer specified primary particle sizes of 7 nm and 0.3 μm, respectively. The particles were introduced into the fuel stream using a seeding apparatus that was developed within the laboratory. The methods for FPI and PIV seeding, image acquisition, and data processing are fully discussed in Refs. 6 and 7, respectively. For the PIV measurements, the field of view of the camera was smaller than the available measurement region, and hence, data were obtained at a series of measurement stations. The time-averaged centerplane velocity contours were then displayed as a juxtaposition of the time-averaged velocity field at each station. Thus, some discontinuities in velocity contours were evident at the edges of the field of view of each measurement station. Excluding flow tracking errors, which Ref. 7 estimated to be generally low, uncertainty in measured instantaneous velocity was estimated to be near 6%. RMS velocity fluctuations (or turbulence intensities) in the fuel plume were close to 10% for the fuel-air mixing case, and for the reacting case were generally in the range of 10 to 60%.

Numerical Technique

As already mentioned, the VULCAN code was adopted for the present investigation. VULCAN is a general-purpose CFD code

that can solve the Reynolds-averaged Navier–Stokes (RANS) equations. It includes a wide variety of physical, thermochemical, and turbulence models. A full description of the code can be found in the literature.[12] Only the specifics of the present application are described here. In a manner similar to Ref. 6, the Mach 2 nozzle and scramjet combustor were solved separately and sequentially; the exit conditions from the nozzle were used as inlet conditions for the combustor. In addition to using a different CFD code, the present numerical model incorporated a finer grid and a more accurate turbulence model than the numerical model of Ref. 6. Because the nozzle and combustor were solved using different approaches, their solution procedure is described separately.

Mach 2 Nozzle

The domain for the Mach 2 nozzle was three dimensional and included the full Y dimension and half of the Z dimension. It extended from $6.23H$ upstream of the throat to the nozzle exit. The grid dimensions were $201 \times 61 \times 49$ ($X \times Y \times Z$), with the entire grid equally divided into 10 blocks. The wall spacing was such that the maximum inner-law variable y^+ was 11.0. To minimize simulation run times, the comparison with the Mach 2 nozzle survey data was performed using a two-dimensional domain. This allowed the effects of boundary conditions, such as the laminar or turbulent state of the boundary layer, to be easily explored. For the two-dimensional domain, the nozzle centerplane was limited in the Y direction to the centerline, and the nozzle grid dimensions were 221×61. In addition, a zone was added downstream of the nozzle exit, and this extended past the nozzle survey measurement plane. This zone modeled the overexpanded freejet region of the nozzle flow issuing into the laboratory. The zone was discretized with grid of dimensions 41×93.

All solid walls were modeled as no slip and isothermal, with a wall temperature of 400 K. Centerplane boundaries were modeled as symmetry conditions. Inflow conditions for the nozzle were assumed to be subsonic, with imposed stagnation conditions given in Table 1. Values of turbulence intensity τ and turbulent-to-laminar viscosity ratio μ_T/μ_L were assumed to be 0.01 and 1.0, respectively. For the three-dimensional case, nozzle wall boundary layers were assumed to be turbulent, and the nozzle outflow plane was modeled as an extrapolation boundary. The boundaries for the freejet zone in the two-dimensional case were modeled as subsonic inflow/outflow at ambient stagnation conditions.

Space integration was performed with Edwards's Low-Dissipation Flux-Split Scheme (LDFSS),[16] with Van Leer limiters and third-order Monotone Upstream-Centered Schemes for Conservation Laws (MUSCL) interpolation. Time integration was performed as fully elliptic using the diagonal-approximate-factorization scheme.[17] The turbulence model used was Wilcox's 1998 k–ω model with wall-matching functions.[18] A turbulent Prandtl number Pr_T of 0.90 was adopted, and the flow was assumed to be a single-specie calorically perfect gas.

The three-dimensional model was run on an SGI Origin 2000, using VULCAN's message-passing-interface capability. Ten R10000, 250-MHz processors were used. A three-grid sequence was used for convergence acceleration. The maximum Courant–Friedrichs–Lewy (CFL) number was five, and the maximum residual of the discretized equations was reduced by four orders of magnitude after approximately 7000 iterations. The two-dimensional nozzle model was run on a single-processor R10000.

Combustor

The three-dimensional domain of the scramjet combustor was discretized over half of the Z dimension by approximately two million control volumes (CVs), nearly equally divided among 48 blocks. Non-C(0) discontinuities (grid lines that are discontinuous across interfaces) among the blocks allowed the grid to be clustered in critical locations, while keeping the total number of CVs to a practical level. Between 68 to 132 CVs were used in the Y direction and 48 to 128 in the Z direction. The maximum y^+ at the walls was approximately 100. The grid was finer than used previously by Ref. 6.

Symmetry conditions were used on the symmetry centerplane. Solid walls were again modeled as no slip, isothermal at 400 K (of the order as that measured in the combustor walls). As already mentioned, the inflow conditions were provided by the three-dimensional nozzle outflow solution. These outflow conditions were set as extrapolation, that is, all variables in inside cells were extrapolated to the boundary cells. The conditions on the fuel-injector nozzle outflow plane were assumed to be uniform, at the values of Table 1, and τ and μ_T/μ_L were assumed to be 0.01 and 1.0, respectively. Unlike the model of Ref. 6, the fuel-injection port was modeled as being round, and an atmospheric exit condition was not imposed at the downstream end of the combustor.

The space and time integration and turbulence model were the same as adopted for the Mach 2 nozzle model. In addition, Wilcox's compressibility correction[18] was used to account for Mach-number effects in turbulent diffusion. The turbulent Schmidt number Sc_T was 0.50, and Pr_T was 0.9.

The flow was modeled as a chemically reacting mixture of thermally perfect gases. A 7-specie/7-reaction model[19] was originally intended to be used. However, because this reaction model did not permit flame holding by the present combustor model, a 4-specie/1-step model was implemented (i.e., O_2, H_2, H_2O, and N_2 with a very high forward-rate constant and a zero-rate backward reaction). This was also required for the model of Ref. 6. For comparison with the fuel-air mixing case of the experiment, a frozen-flow model was used with two thermally perfect species: H_2 and a single-specie model for air that was available in VULCAN.

The scramjet numerical model was run on 48 500-MHz processors. Grid sequencing was again used for convergence acceleration and to obtain estimates of grid convergence. The maximum CFL number was five. A total of 30,000 iterations were run (10,000 of them in the fine sequence). It was found that it was not possible to lower the residual by more than a couple orders of magnitude. Therefore, convergence was considered to have been achieved when the wall-pressure distribution in the combustor remained unchanged after several hundred iterations.

Results and Discussion

Mach 2 Nozzle Study

Results of the Mach 2 nozzle survey investigation are presented in Fig. 3. Figure 3a presents a schlieren image of the survey probe while in the nozzle flow. The shadows of the probe cantilever arm and the total temperature probe (left) and pitot tube (right) are clearly evident. The vent holes of the total temperature probe are also visible. The horizontal shadow across the lower boundary of the image shows the exit plane of the Mach 2 nozzle. Three lines have been overlaid over the image to mark the nozzle centerline and walls.

Bow shocks from the total temperature probe and pitot tube are clearly evident in the image. A lack of interaction between these shocks confirms that the two tubes are sufficiently separated. The nozzle flow displays the characteristics of a rectangular overexpanded jet. An oblique shock and shear layer on either side of the jet are clearly defined. The oblique shocks exhibit a small amount of upstream interaction as they emanate from a point slightly upstream of the nozzle-exit plane. Extrapolation of these shocks to the nozzle walls indicates a distance of upstream interaction of 0.2H.

A Mach-number contour plot, generated using the two-dimensional nozzle model, is presented in Fig. 3c. The plot is displayed using the same dimensional scale as Fig. 3a, and the measurement plane is depicted. The simulation was performed assuming a turbulent nozzle wall boundary layer. The numerical model predicts an exit Mach number in the range of 2.04 to 2.07, and this compares favorably with the inviscid, area-ratio based estimate in Table 1. The Mach-number plot also shows shock angles and an upstream interaction extent ($0.35H$) that are similar to the experimental results. When the numerical model was run using a laminar boundary layer in the nozzle, upstream interaction extended four times further up into the nozzle. Thus, given the similarity between experiment and the model using a turbulent boundary layer, the boundary layer in the experiment is most likely turbulent. This result alleviates previous uncertainty as to the state of the nozzle boundary layer. Prior to

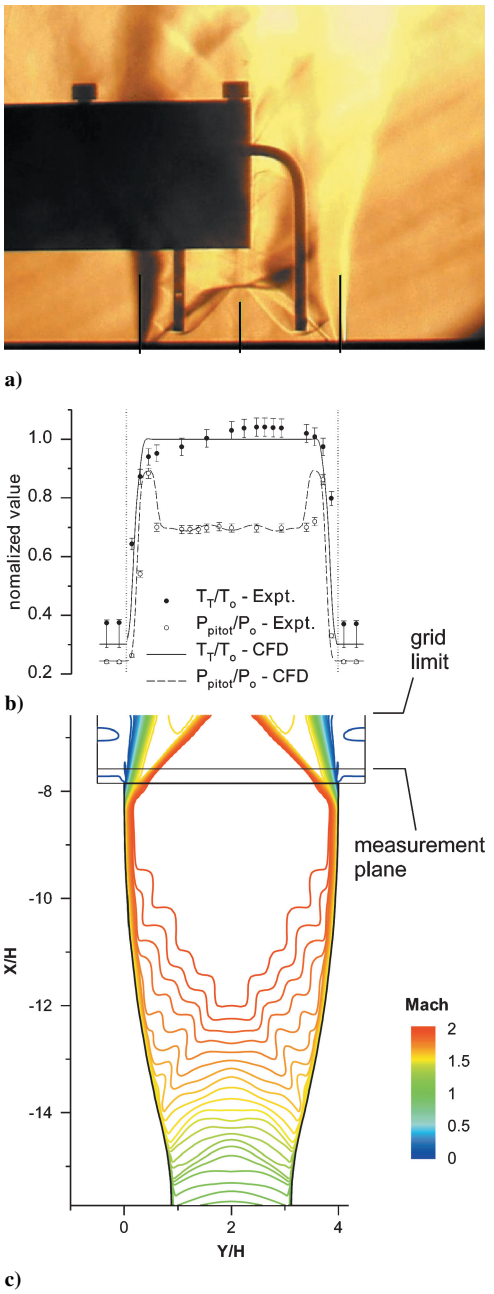

Fig. 3 Mach 2 nozzle experimental and numerical investigation at $Z/H = 0$: a) schlieren of flow and survey probe; b) total temperature and pitot-pressure survey, $T_0 = 1030$ K and $P_0 = 415$ kPa; and c) numerically predicted Mach-number distribution (figures share same horizontal scale).

shock interaction near the exit of the nozzle, the numerical model predicts a boundary-layer thickness on the order of 1 mm.

Experimental and numerical profiles of total temperature T_t and pitot pressure P_{pitot} are presented in Fig. 3b for the $Z/H = 0$ plane. Temperature and pressure have been normalized by the measured facility stagnation temperature T_0 and stagnation pressure P_0, respectively. The pitot-pressure measurements and CFD show very good agreement. Across the center of the jet, both experiment and CFD show a pressure ratio P_{pitot}/P_0 near 0.7. To within experimental uncertainty, this is equal to the theoretical level predicted using one-dimensional normal shock theory and the conditions of Table 1. There is also very good agreement between experimental and numerical pitot-pressure levels at the edges of the jet. The peaks in pitot pressure that are evident at the edges of the jet reflect the intersection of the measurement plane with the oblique shocks. Thus, the strength and position of the shocks are captured well by the numerical simulation. The agreement between the experimental and numerical pitot-pressure profiles serves to confirm the choice of a turbulent boundary layer on the nozzle walls in the numerical modeling. Pitot pressure was also measured on other Z planes. These measurements showed that the pitot-pressure profile of the nozzle was two dimensional within the region bounded by the oblique shock waves.

Experimental and numerical profiles of the flow total temperature are also presented in Fig. 3b. In contrast to the CFD, an asymmetrical feature is evident in the experimental results. It was confirmed that this feature was not induced by the asymmetrical nature of the survey probe by obtaining a series of measurements with the probe mounted on the opposite side of the nozzle. In this case, total temperature measurements generally agreed with those in Fig. 3b to within experimental uncertainty. It is proposed that the observed asymmetry reflects an asymmetric temperature profile generated by the facility heater. Such a profile could be produced by a cold-air intrusion in the heater tank, between the cold-air outer annular section and the slightly lower pressure, high-temperature heater core. Experimental levels of T_t/T_0 reach levels above unity. This is consistent with a cold-air intrusion reducing the air temperature in the heater tank at the location of facility stagnation temperature measurement.

Experimental measurements of total temperature on other Z planes exhibited that, neglecting wall effects, the total temperature profile of the nozzle was approximately two dimensional. However, a decrease in total temperature, on the order of that observed in Fig. 3b at low Y, was evident in the nozzle corner at low Y and negative Z. Thus, this corner may also be affected by a cold-air intrusion. Given the maximum differences between experimental and numerical profiles in Fig. 3b are on the order of 5%, the asymmetrical profile in temperature is not expected to significantly affect the experimental and numerical comparisons that follow herein.

Combustor Study

Pressure and Mach-Number Distributions

Figure 4 presents the experimental and numerical pressure distributions, along the injection wall, for the cases of fuel-off, fuel-air mixing, and fuel-air reacting. Pressure is normalized using the measured nozzle-exit pressure for fuel off ($P_{\text{ref}} = 48$ kPa) and is plotted as a function of the normalized distance from the base of the ramp fuel injector. For the fuel-off case in Fig. 4a, the presence of ramp-generated shocks and expansion waves leads to significant fluctuations in the streamwise pressure distribution. It can be seen that there is good agreement between the experimental and numerical results for this case. As the numerical model did not include an atmospheric exit condition at the downstream end of the combustor, the model does not capture the pressure rise to 1 atm, which occurs downstream of $40H$ in the measurements. However, this does not affect interpretation and comparison of the results upstream of $40H$.

Referring to Fig. 4b, when fuel is introduced into the combustor, but not ignited, the pressure distribution is similar to the fuel-off case. The pressure levels in the combustor, for both cases, are consistent with supersonic flow. As for the fuel-off case, the numerical model generally captures the ramp-generated shock and expansion waves. Comparisons of the experimental and numerical pressure distributions for the fuel-off and mixing cases were not considered in the previous study of Ref. 6.

Once fuel is ignited, there is a significant pressure rise in the combustor. This is depicted in Fig. 4c. Referring to the experimental results, the pressure levels at the nozzle exit ($-7H$) and on the ramp face ($-5H$) are the same as for the fuel-off and mixing cases; hence, the inflow to the combustor is supersonic. Numerical predictions of the streamwise pressure distribution are also presented in Fig. 4c for two of the three grid levels used for the grid sequencing. The fact that the distributions are very close to each other suggests that the calculations are close to being grid converged. Comparing the fine-grid results with the experimental measurements, it can be seen that the model accurately predicts the wall pressure between -7 and 12 ramp heights from the base of the fuel injector. The agreement in this region is an improvement over the previous simulation of Ref. 6. Downstream of $12H$, the numerical model overpredicts the

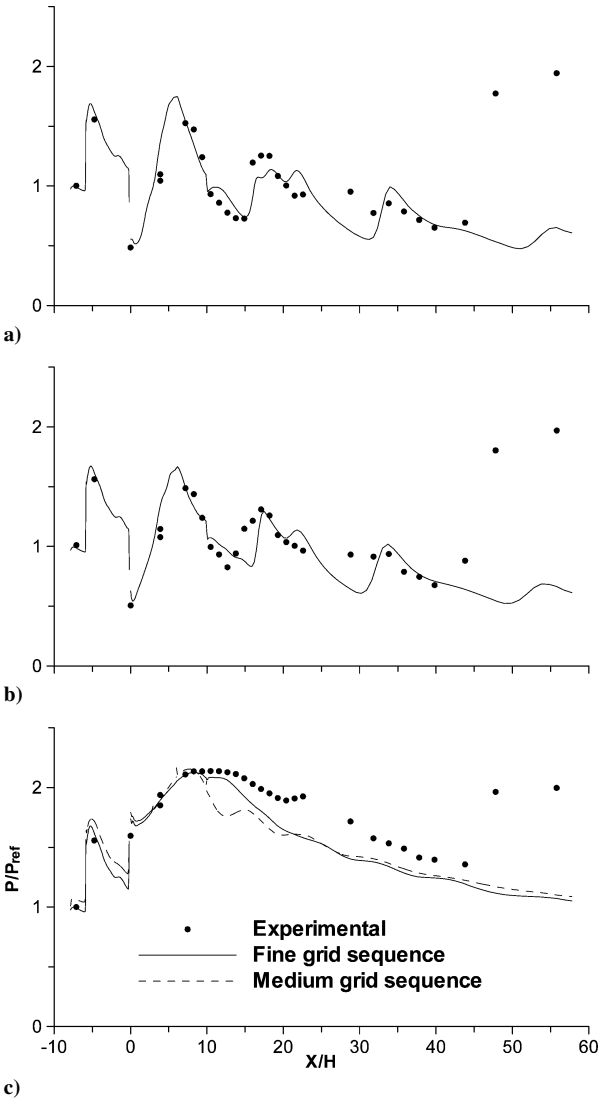

Fig. 4 Experimental and numerical wall-pressure distribution for a) fuel-off, b) fuel-air mixing, and c) fuel-air reacting, $P_{ref} = 48$ kPa; experimental uncertainty is $\pm 2\%$.

level of expansion, or acceleration, that occurs along the 2.9-deg diverging section of the wall. The numerical model of Ref. 6 also overpredicted expansion in this region.

The numerically predicted centerplane Mach-number contours, presented in Fig. 5 for the cases of fuel-air mixing and reacting, support the findings drawn from the pressure distributions. For the mixing case in Fig. 5a, the flow remains supersonic, except for the low-pressure, recirculation region immediately downstream of the ramp base. The underexpanded nature of the hydrogen fuel jet, which results in a barrel shock and Mach disk, is also evident. For the fuel-air reacting case in Fig. 5b, the heat release of combustion leads to a large subsonic, or thermally choked, region along the injection wall. The inflow to the combustor and the region along the upper portion of the duct, however, remains supersonic. This was also observed by Ref. 6. Crossflow contours of Mach number (not shown) predicted that the supersonic region also extended along the side walls of the duct. The expansion downstream of $12H$, which was observed in the numerical pressure distribution in Fig. 4c, is consistent with the flow near the injection wall accelerating from Mach 0.6 to Mach 1.2. The hydrogen fuel jet Mach-number profile for the reacting case again reflects that of an underexpanded jet. However, as the jet is now issuing into a higher pressure field, compared to the mixing case, less jet expansion and lower Mach numbers are evident. Interestingly, for the reacting case, the high-Mach-number region of the hydrogen jet exhibits greater penetration into the freestream than for the mixing case, despite the fact

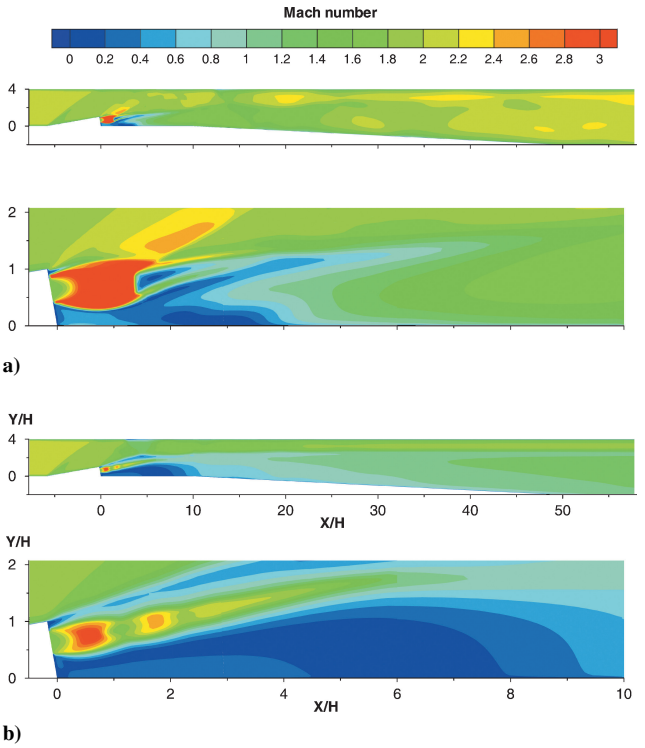

Fig. 5 Numerically predicted Mach-number distribution on the centerplane. Full domain and ramp base region displayed for a) fuel-air mixing and b) fuel-air reacting.

that the mixing case jet expands into a lower pressure, higher Mach number freestream, and expands to higher Mach numbers. This issue is addressed in the following discussion.

Fuel Plume Velocity Field and Distribution

The time-averaged fuel plume velocity field, for the cases of fuel-air mixing and reacting as measured by Ref. 7 using PIV, are presented in Figs. 6a and 6c, respectively. As identified by Ref. 7, the fuel plume exhibits a near-field high-speed core that extends approximately four and six ramp heights downstream of the fuel injector for the mixing and reacting cases, respectively. For the mixing case, this core penetrates to a distance of approximately $1.3H$ from the injection wall at $X/H \approx 4$. Downstream of this point, in the far field of the fuel plume the velocity approaches the calculated freestream velocity in Table 1 of 1030 m/s. Compared to the mixing case, the high-speed core of the reacting fuel jet exhibits higher velocity magnitudes and penetrates further into the flow-reaching $Y/H = 1.8$ at $X/H \approx 6$. Based on the work of Ref. 20 with subsonic combusting jets, Ref. 7 postulated that the higher velocity of the reacting jet was caused by heat-release-induced expansion in the jet. This process has the effect of maintaining streamwise velocities and reducing entrainment of the lower speed freestream into the fuel jet. A similar effect might be at work in the present supersonic case. Downstream of $X/H = 6$, velocity magnitudes are lower than measured for the mixing case. This is because of the heat release of combustion leading to thermal choking.

Referring to the numerical results for the mixing case, in Fig. 6b, it can be seen that the numerically predicted velocity magnitude in the jet far field ($X/H > 4$) is similar to that measured, particularly at high X/H. However, the numerically predicted velocity is higher in the near field. In addition, the numerical fuel jet velocity field, immediately downstream of $X/H = 1$, reflects the jet barrel shock and Mach disk identified in Fig. 5a. A thin section of the high-speed core persists downstream to $X/H \approx 3.8$ and $Y/H \approx 1.3$. This feature is a remnant of the shear layer associated with the barrel shock of the underexpanded jet. Interestingly, the lower portion of the shear layer, which is just visible at $X/H = 2$, $Y/H = 0.7$, is very weak. Such features may be reflected in the experimental measurements of Fig. 6a. However, it is not clear if differences are caused by

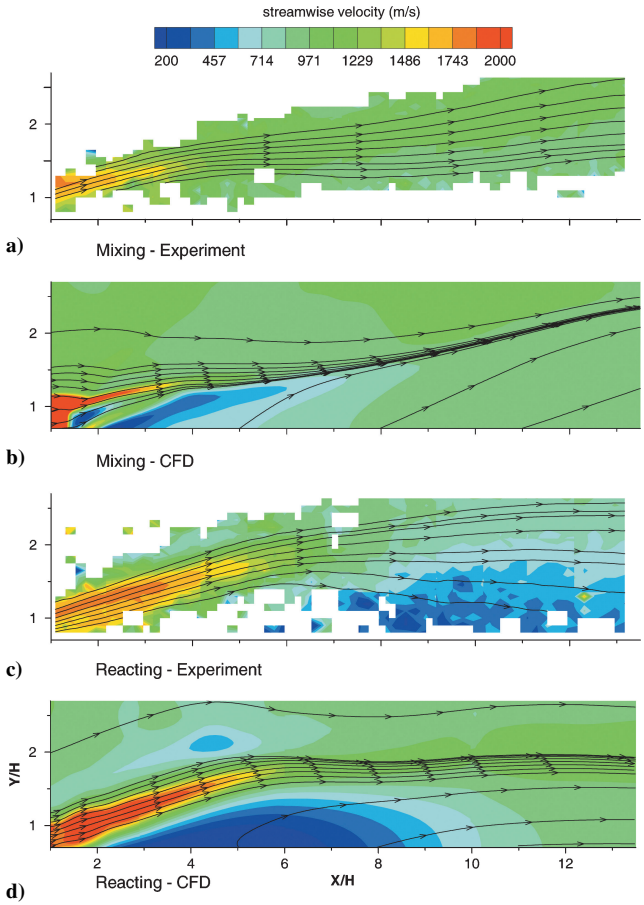

Fig. 6 Centerplane streamwise velocity and interpolated streamlines: a) measured and b) numerically predicted for fuel-air mixing, and c) measured and d) numerically predicted for fuel-air reacting (Note: *X*:*Y* scale ratio not 1:1).

particle tracking errors in the measurements or inadequacies of the numerical model. The former reach a maximum in regions of high fluid acceleration or deceleration.[7] In any case, penetration and axial streamwise extent of the upper portion of the shear layer are consistent with that for experiment in Fig. 6a. Comparing the streamlines that have been overlaid onto Figs. 6a and 6b, it can be seen that the numerically predicted streamlines do not match those experimentally observed for the mixing case. In the experimental velocity field, streamlines initially lift off the injection wall and then turn to match the freestream direction. The streamlines then turn back away from the wall and continue to diverge. The numerically predicted streamlines take a similar course. However, they can be seen to converge in a manner that would seem unrealistic. The source of the observed convergence is uncertain.

Figure 6d presents the numerically predicted contours for the fuel-air reacting case. Comparing this with the measurements in Fig. 6c, it can be seen that the overall velocity fields are similar, but the numerical magnitudes are generally higher. In the near field, high-speed core streamwise extent, penetration distance, and angle are almost the same. Importantly, the magnitude of each of these parameters that is numerically predicted for the mixing case is lower than for the numerical reacting case. Thus, the CFD model is capturing the same effects observed in the experimental measurements, namely, a slower streamwise decay in the fuel-jet velocity and higher penetration when combustion takes place. The numerical model indicated that the static temperature of the fuel jet, and hence the speed of sound, was relatively uniform and was approximately the same for the mixing and reacting cases. Therefore, the velocity field effects just identified are reflected in the Mach-number contours of Fig. 5.

Comparing the far field of the numerical reacting fuel plume velocity ($X/H > 6$) in Fig. 6d with that of experiment in Fig. 6c, it can be seen that the model does not predict the extent of velocity reduction that results because of thermal choking. This suggests that the CFD is not able to adequately match the amount of heat release. The reduced heat release might also be manifested in the stream traces of Fig. 6d, which tend to converge, rather than diverge (as in the measurements of Fig. 6c). However, as for the numerical mixing streamline comparison, the cause of the discrepancy with experiment is not fully understood.

Based on the velocity comparison in Ref. 7, the present numerical model performs better than the model of Ref. 6 when predicting the reacting flowfield. This finding is based largely on the fact that the penetration of the jet high-speed core now matches experiment. However, the level of velocity magnitude overprediction and streamtrace divergence underprediction is still similar.

The experimental and numerical fuel plume distribution is now examined. Time-averaged crossflow fuel plume images, measured for the case of fuel-air mixing, are presented in Fig. 7. The ramp-induced counter-rotating vortices can be clearly seen to be imparting a "kidney"-shaped cross section on the fuel plume. As is expected, the location of the fuel plume along $Z/H = 0$ is consistent with the location of the PIV measurements of Fig. 6. From Fig. 7, it can be seen that the fuel plume size and penetration increases with distance from the fuel injector. On the centerplane, this is consistent with the streamline divergence and lift observed in Fig. 6.

In a manner similar to Ref. 6, Fig. 7 also presents numerically predicted contours of total hydrogen atom mass fraction. This includes all hydrogen in the form of H_2 and H_2O that, in the experiment, is effectively tagged by the seed particles. It can be seen that the numerically predicted plume shape is similar to, but is generally smaller than experiment. On the centerplane, the plume axial growth and penetration are also underpredicted at each plane. This is consistent with the differences already observed in the streamlines of Figs. 6a and 6b. Given that the plume shape is approximately matched by the CFD, it would appear that the mixing caused by the ramp-induced vortices is qualitatively matched. Given that the plume size and penetration is underpredicted, turbulent mixing of the numerical model may also be underpredicted.

Experimental and computational fuel plume distributions for the case of fuel-air reacting are presented in Fig. 8 for the same measurement planes. Comparing the reacting and mixing experimental plumes, the heat release of combustion generally leads to a larger fuel plume and increased plume penetration, with a distinct difference in size at $X/H = 3$ that is not as apparent. On the duct centerplane, this is consistent with the behavior of the streamlines of Figs. 6a and 6c, namely, more penetration of the high-speed core of the jet, and more divergence of the streamlines when combustion takes place. These differences are greater as the flow proceeds downstream. Referring again to Fig. 8, comparison of the numerically predicted reacting plumes with experiment yields conclusions similar to the mixing results. The experimental plume shapes are approximated, and the plume size, penetration, and centerplane axial growth are generally underpredicted by the model (although, at $X/H = 3$, the numerical plume does appear larger). Reference 6 similarly obtained underprediction using the preceding numerical model. Again, on the centerplane the fuel plume traits are reflected in the differences in the streamlines of Figs. 6c and 6d, that is, convergence and reduced penetration of the numerical streamtraces, with greater deviation from experiment in the streamwise direction. Comparing the numerical results in Figs. 7 and 8, the model predicts a larger fuel plume and increased penetration when combustion takes place, which is similar to experiment. This is in contrast to the deficiency of the model examined in Ref. 6.

Referring again to Figs. 7 and 8, both the experimental and numerical fuel plumes display less of a distinct kidney shape when combustion takes place. Based on experimental results, Ref. 6 proposed that this indicated that the effects of the ramp-induced vortices are diminished when combustion takes place. Thus, it would appear that this is an effect which the present numerical model is able to capture, and this is in contrast to the numerical model examined by Ref. 6. Although the effects of the ramp-induced vortices would appear to be simulated by the numerical model for both the mixing

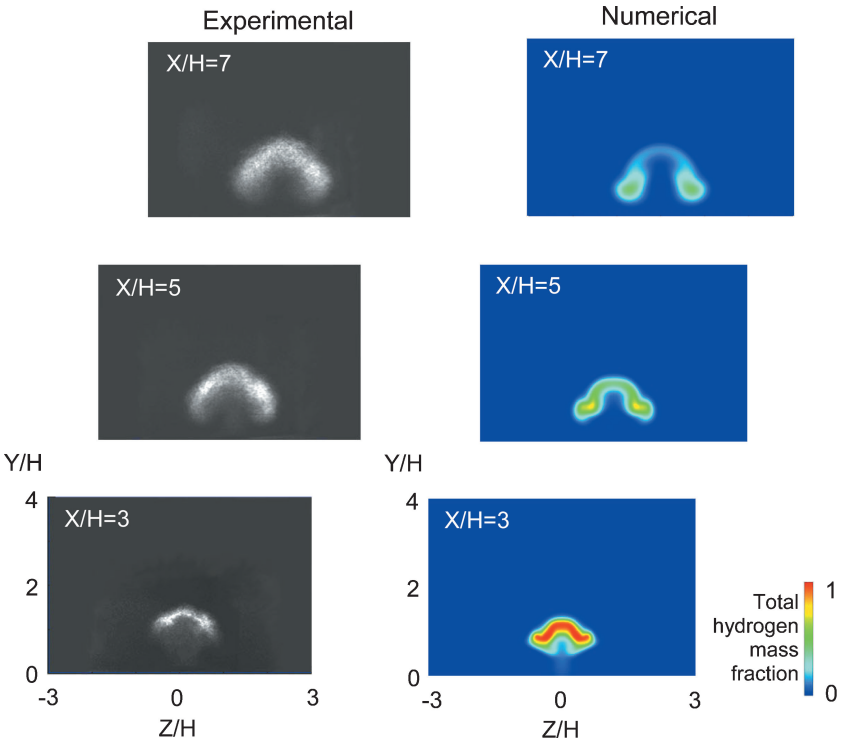

Fig. 7 Experimental and numerical crossflow fuel plume distribution for fuel-air mixing.

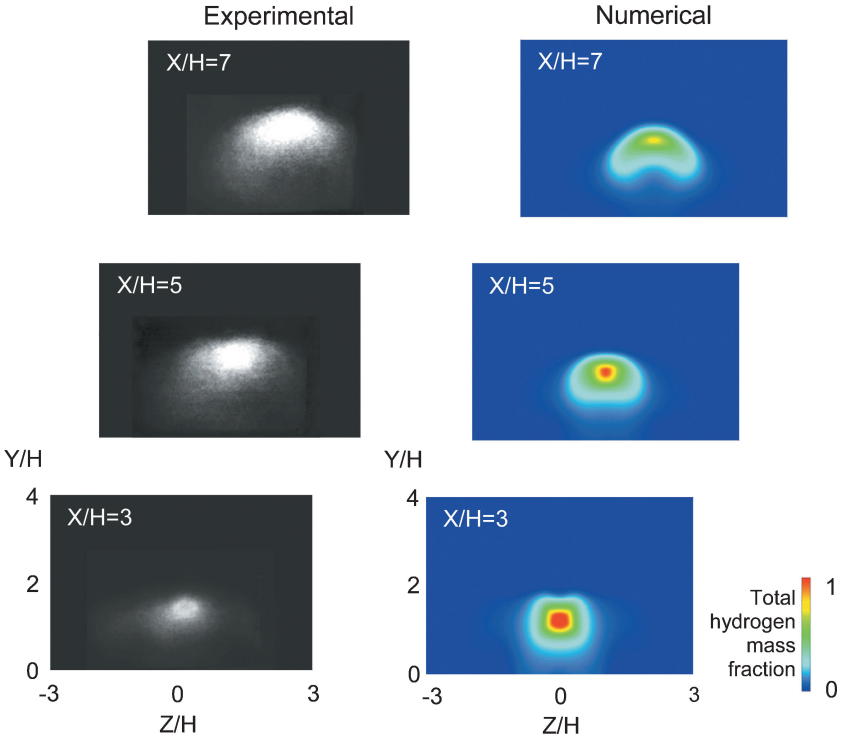

Fig. 8 Experimental and numerical crossflow fuel plume distribution for fuel-air reacting.

and reacting cases, the general smaller size, reduced penetration, and retarded centerplane axial growth of the numerically predicted reacting plume indicates less predicted heat release.

Conclusions

A study of a direct-connect Mach 2 hydrogen-air combustor with a 10-deg unswept-ramp fuel injector has been performed. Both the experimental and numerical aspects of the study enabled examination of the cases of fuel-air mixing and fuel-air reacting. Thus, the effect of heat release of combustion on the fuel-air mixing process could be isolated. The investigation of the fuel-air mixing and combustion processes incorporated experimental data that included combustor wall-pressure distributions and FPI and PIV measurements. Based on the FPI and PIV data, the numerical model predicted the fuel plume shape well for both the mixing and reacting cases. The model also predicted a larger fuel plume and increased penetration for the reacting case than for the mixing case, which was

in general agreement with experiment. In addition, the penetration of the fuel jet's high-speed core was matched for the reacting (and mixing) case. Agreement in the upstream third of the combustor pressure distribution was also better than previously obtained. The preceding results are an improvement over the previous modeling of the investigators.

Two main findings can be drawn from the present investigation. First, the numerical model underpredicts the level of turbulent mixing, and second the model underpredicts the level of heat release of combustion. Evidence of underprediction of turbulent mixing stems from the fuel-air mixing results. When combustion was precluded, the model generally underpredicted the fuel plume size and penetration. In addition, the numerically predicted streamlines of the plume did not diverge, providing further evidence of reduced entrainment of the freestream through turbulent mixing. As the numerical fuel plume shape approximated that of experiment for the mixing case, the model was able to qualitatively capture the level of mixing generated by the ramp-induced vortices. Thus, the level of mixing enhancement of large-scale structures in the flow, unlike mixing induced through smaller-scale turbulence, was qualitatively matched.

The fuel-air reacting comparisons yielded evidence of numerical underprediction of heat release. The numerical model predicted a reduced pressure rise throughout much of the combustor, less thermal choking in the velocity far field of the fuel plume, no divergence of plume streamlines, and less penetration of streamlines, despite higher predicted velocities of the plume. Reduced plume size and penetration were also generally numerically predicted for the reacting case. In addition, only a one-step chemistry model, rather than a more realistic seven-reaction model, was able to numerically flame hold.

Numerical underprediction of turbulent mixing and heat-release points to inadequacies in the adopted turbulence model and chemistry model and the turbulence/chemistry interaction. The amount of heat released by a one-step chemistry model would be expected to be more than the actual complex, higher-order combustion process of the experiment. Thus, reduced, heat release of the numerical model can be attributed to reduced turbulent mixing or inadequacies of the turbulence model and not to the chemistry model. Such a strong coupling between heat release and turbulent mixing might largely be the result of the one-step chemistry model. However, factors such as 1) combustor inlet enthalpies below that required for fuel autoignition and 2) relatively low fueling equivalence ratios might also play a role.

Accuracy of the present numerical model can therefore be improved through developmental work on the turbulence modeling. This not only includes a detailed examination of the appropriateness and implementation of the Wilcox turbulence model and compressibility correction adopted herein, but also the effect freestream and injected fuel turbulence levels, for example, have on the fuel-air mixing process. This level can be quantified through further experimental investigation, particularly using techniques, such as PIV, which enable turbulence intensity levels to be quantified.

Acknowledgments

This research was funded by NASA through Grant NAG-1-02019 with C. R. McClinton and D. E. Reubush of the NASA Langley Research Center as technical monitors. The authors would also like to thank John Robichaux of the University of Virginia for obtaining the schlieren image of the nozzle survey probe and for providing assistance in the preparation of the manuscript figures. Thanks also to Matt Daniell of the University of Virginia for providing assistance with the fuel plume image analysis and in the preparation of figures.

References

[1]McClinton, C. R., Ferlemann, S. M., Rock, K. E., and Ferlemann, P. G., "The Role of Formal Experiment Design in Hypersonic Flight System Technology Development," AIAA Paper 2002-0543, Jan. 2002.

[2]Huebner, L. D., Rock, K. E., Ruf, E. G., Witte, D. W., and Andrews, E. H., Jr., "Hyper-X Flight Engine Ground Testing for Flight Risk Reduction," *Journal of Spacecraft and Rockets*, Vol. 38, No. 6, 2001, pp. 844–852.

[3]McClinton, C. R., Rausch, D. R., Sitz, J., and Reukauf, P., "Hyper-X Program Status," AIAA Paper 2001-1910, April 2001.

[4]Krauss, R. H., Gauba, G., Whitehurst, R. B., Quagliaroli, T. M., and Laufer, G., "Experimental and Numerical Investigation of Steam-Vitiated Supersonic Hydrogen Combustion," AIAA Paper 96-0856, Jan. 1996.

[5]Gauba, G., Klavuhn, K. G., McDaniel, J. C., Victor, K. G., Krauss, R. H., and Whitehurst, R. B., "OH Planar Laser-Induced Fluorescence Velocity Measurements in a Supersonic Combustor," *AIAA Journal*, Vol. 35, No. 4, 1997, pp. 678–686.

[6]Goyne, C. P., McDaniel, J. C., Quagliaroli, T. M., Krauss, R. H., and Day, S. W., "Dual-Mode Combustion of Hydrogen in a Mach 5, Continuous-Flow Facility," *Journal of Propulsion and Power*, Vol. 17, No. 6, 2001, pp. 1313–1318.

[7]Goyne, C. P., McDaniel, J. C., Krauss, R. H., and Day, S. W., "Velocity Measurement in a Dual-Mode Supersonic Combustor Using Particle Image Velocimetry," AIAA Paper 2001-1761, April 2001.

[8]Rodriguez, C. G., White, J. A., and Riggins, D. W., "Three-Dimensional Effects in Modeling of Dual-Mode Scramjets," AIAA Paper 2000-3704, July 2000.

[9]Rodriguez, C. G., "Asymmetry Effects in Numerical Simulation of Supersonic Flows with Upstream Separated Regions," AIAA Paper 2001-0084, Jan. 2001.

[10]Rodriguez, C. G., "Computational Fluid Dynamics Analysis of the Central Institute of Aviation Motors/NASA Scramjet," *Journal of Propulsion and Power*, Vol. 19, No. 4, 2003, pp. 547–555.

[11]"GASP Version 3—User's Manual," Aerosoft, Inc., Blacksburg, VA, March 1997.

[12]White, J. A., and Morrison, J. H., "A Pseudo-Temporal Multi-Grid Relaxation Scheme for Solving the Parabolized Navier–Stokes Equations," AIAA Paper 99-3360, June 1999.

[13]Krauss, R. H., McDaniel, J. C., Scott, J. E., Whitehurst, R. B., Segal, C., Mahoney, G. T., and Childers, J. M., "Unique, Clean-Air, Continuous-Flow, High-Stagnation-Temperature Facility for Supersonic Combustion Research," AIAA Paper 88-3059, July 1988.

[14]Krauss, R. H., and McDaniel, J. C., "A Clean Air Continuous Flow Propulsion Facility," AIAA Paper 92-3912, July 1992.

[15]Albertson, C. W., and Bauserman, W. A., Jr., "Total Temperature Probes for High-Temperature Hypersonic Boundary-Layer Measurements," NASA TM 4407, March 1993.

[16]Edwards, J. R., "A Low-Diffusion Flux-Splitting Scheme for Navier–Stokes Calculations," *Computers and Fluids*, Vol. 26, No. 6, 1997, pp. 635–659.

[17]Pulliam, T. H., and Chaussee, D. S., "A Diagonal Form of an Implicit Approximate-Factorization Algorithm," *Journal of Computational Physics*, Vol. 39, No. 2, Feb. 1981, pp. 347–363.

[18]Wilcox, D. C., *Turbulence Modeling for CFD*, 2nd ed., DCW Industries, Inc., La Canada, CA, 1998.

[19]Drummond, J. P., Rogers, R. C., and Hussaini, M. Y., "A Detailed Numerical Model of a Supersonic Reacting Mixing Layer," AIAA Paper 86-1427, June 1986.

[20]Takagi, T., Shin, H., and Ishio, A., "Properties of Turbulence in Turbulent Diffusion Flames," *Combustion and Flame*, Vol. 40, 1981, pp. 121–140.